NJC
New Journal of Chemistry
A journal for new directions in chemistry

Accepted Manuscript

This article can be cited before page numbers have been issued, to do this please use: G. Deviga, S. Ravi, S. P. Anthony and M. Mariappan, *New J. Chem.*, 2025, DOI: 10.1039/D5NJ02527C.

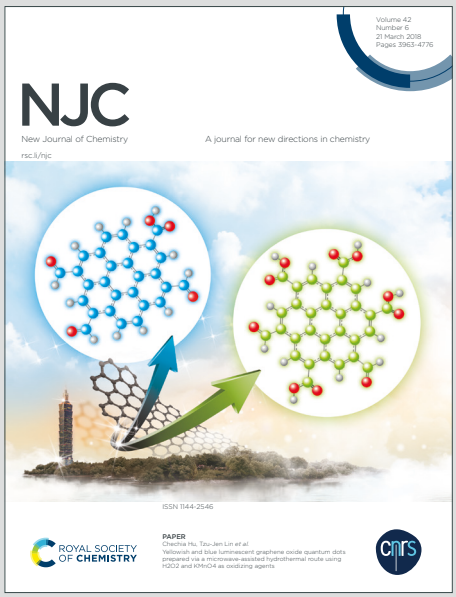

This is an Accepted Manuscript, which has been through the Royal Society of Chemistry peer review process and has been accepted for publication.

Accepted Manuscripts are published online shortly after acceptance, before technical editing, formatting and proof reading. Using this free service, authors can make their results available to the community, in citable form, before we publish the edited article. We will replace this Accepted Manuscript with the edited and formatted Advance Article as soon as it is available.

You can find more information about Accepted Manuscripts in the Information for Authors.

Please note that technical editing may introduce minor changes to the text and/or graphics, which may alter content. The journal's standard Terms & Conditions and the Ethical guidelines still apply. In no event shall the Royal Society of Chemistry be held responsible for any errors or omissions in this Accepted Manuscript or any consequences arising from the use of any information it contains.

View Article Online
DOI: 10.1039/D5NJ02527C

Journal Name

ARTICLE

Electron-Deficient P(V) Corroles as Dual-Functional Materials for Selective Fluoride Detection and Photocatalysis

Received 00th January 20xx,
Accepted 00th January 20xx

DOI: 10.1039/x0xx00000x

www.rsc.org/

Govindan Deviga,[a] Sasikala Ravi[b], Savarimuthu Philip Antony[b], Mariappan Mariappan[a*]

Phosphorus(V) corroles incorporating electron-withdrawing groups and π-extended meso-aryl fluorophoric substituents (P1 and P2) were synthesized and characterized using various basic spectroscopic tools including ^{1}H NMR, ^{31}P NMR, and ESI mass spectrometry. The P(V) corroles demonstrated selective fluoride ion (F^-) sensing by distict colorimetric and fluorometric changes among a series of anions, with detection limits of 0.39 µM for P1 and 0.34 µM for P2. Spectroscopic techniques including FT-IR, ESI mass spectrometry, along with electrochemical measurements, established a 1:1 binding stoichiometry between the corrole and F^- through hydrogen bonding interactions. Computational studies (DFT and TD-DFT) supported the experimental observations. The practical application of these sensors was established through solid-state detection and smartphone-assisted RGB analysis. Furthermore, P1 and P2 functioned as effective photocatalysts for the aerobic oxidation of sulfides to sulfoxides using molecular oxygen as the sole oxidant. Mechanistic investigations revealed the involvement of molecular oxygen in the photocatalytic cycle. These findings highlight the dual functions of P(V) corroles as both sensitive F^- probes and efficient photocatalysts.

Introduction

The detection of environmental pollutants and biological species has attracted significant attention due to the critical need for quantitative analysis in environmental monitoring and public health.[1] Among these, anion sensing, particularly F^- detection is of great importance. F^- ion, the smallest anion with a high charge density, has been extensively researched due to its significant role in numerous biological, industrial, and medical applications. While trace amounts of F^- offer health benefits, such as promoting dental integrity and bone mineralization, excessive exposure can lead to severe health complications, including fluorosis, urolithiasis, neurotoxicity, and carcinogenic effects.[2,3] The potential toxicity of F^- underscores the critical need for highly sensitive, real-time detection methodologies capable of quantifying even trace amounts, thereby enabling effective exposure monitoring and health risk prevention.[4] Among the various techniques developed for anion sensing, chemical sensors offer distinct advantages, including operational simplicity and efficient detection capabilities. Notably, multifunctional colorimetric sensors enable anion identification through observable changes in the analyte, facilitated by selective binding interactions.[5,6] Designing sensor molecules with the capability of NIR excitation/emission, greater stability in the sensing environment and reproducibility is of notable contemporary importance.[1]

Sulfur-based organic compounds, such as sulfides, sulfoxides, and sulfones, constitute important structural motifs in numerous natural products, biologically active molecules, medicinal agents, agrochemicals, and advanced organic materials.[7] Sulfoxide functional groups serve as crucial structural motifs in synthetic organic chemistry[8,9] and pharmacologically active compounds, featuring prominently in commercially approved drugs such as omeprazole, modafinil, and sulindac.[10-12] Significant methodological advances have emerged in recent decades for sulfoxide synthesis, encompassing hydrogen peroxide-mediated oxidation, transition metal-catalyzed transformations, organocatalytic conversion and photochemical oxidation methods. However, those methods require stoichiometric chemical oxidants and metal catalysts.[13-15] To address these challenges, metal-free catalytic systems utilizing molecular oxygen have emerged as a sustainable alternative for sulfoxide synthesis.[16]

Corroles are synthetic analogues of porphyrins that have emerged as particularly important macrocyclic compounds due to their unique structural and photophysical properties.[17] Similar to porphyrins, corroles are tetrapyrrole macrocycles with an 18-π-electron aromatic system. However, their structure features a smaller 23-atom core due to a direct connection between two pyrrole rings.[18] Corroles exhibit distinctive coordination chemistry along with enhanced optical characteristics, including broader absorption and emission in

[a] Department of Chemistry, SRM Institute of Science and Technology (SRMIST), Kattankulathur, Chennai 603203, Tamil Nadu, India.
[b] School of Chemical & Biotechnology, SASTRA Deemed University, Thanjavur 613401, Tamil Nadu, India.

† Footnotes relating to the title and/or authors should appear here.
Electronic Supplementary Information (ESI) available: ^{1}H NMR; ESI mass spectra; photophysical properties table; bond table; absorption and emission titrations. See DOI: 10.1039/x0xx00000x

the visible spectrum and larger Stokes shifts. These advantageous properties have enabled their successful application across multiple fields, including catalysis, photodynamic therapy, cellular imaging, solar energy conversion, and chemical sensing applications.[19-22] Corrole-based complexes have been studied for detecting a wide range of substrates and efficient photocatalysts for organic conversions, due to their favorable photophysical and redox properties.[23] In recent years, significant progress has been made in designing p-block corrole-based sensors, showcasing their sensing abilities. Lodeiro and co-workers have investigated different gallium(III) corroles for identifying cyanide and F^- ions.[24] Michalska and co-workers developed a silicon(IV) corrole incorporated PVDF membrane, which functions as a fluorescence "turn-on" sensor for F^- detection.[25] Similarly, Lvova and co-workers developed a paper-based optode incorporating silicon(IV) corrole specifically for detecting F^- ions.[26] Elements under groups 14 and 15 have established properties of redox activity. Mahammed et.al employs phosphorus corroles as triplet-state photosensitizers for the Aza Henry reaction (oxidative coupling of benzylamine).[27] Literature reports have explored bismuth(III) corrole and antimony corrole complexes as effective photocatalysts for singlet oxygen-mediated sulfoxidation reactions.[28,29]

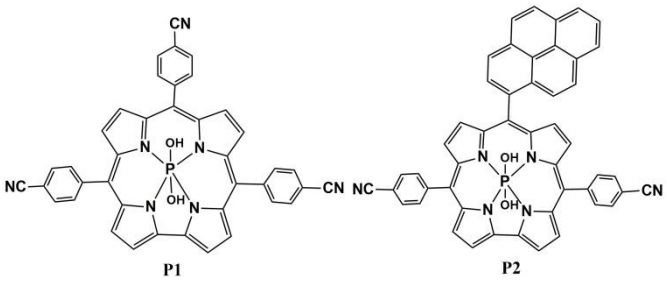

Chart 1: Structures of P1 and P2

Behind this backdrop, we have synthesized two phosphorus(V) corroles (P1 and P2; Chart 1), incorporating meso-substituents with electron-withdrawing (4-cyanophenyl) and π-extended (pyrene) characteristics, tailored for dual applications. Phosphorous corroles are highly fluorescent and have been widely known for their application as photosensitizers, imaging probes in biological applications, sensors and photocatalysts. These synthesised P(V) corroles function as highly selective chemosensors for the detection of F^- ions. Among a panel of tested anions, F^- elicited a distinguishable color change, which was systematically investigated through UV-Vis. spectroscopy, steady-state fluorescence titrations, and electrochemical measurements. The experimental findings were further substantiated by DFT and TD-DFT calculations. In addition, P1 and P2 exhibited pronounced catalytic efficiency in the sulfoxidation of thioanisole under environmentally benign conditions. These results underscore the potential applicability of phosphorus corroles in both anion sensing and sustainable catalysis.

Experimental section

General Information

All the chemicals we used for the preparation of phosphorous corrole and tetrabutylammonium salts were purchased from Avra and SRL chemicals. Tetrabutylammonium cyanide salt was purchased from Sigma Aldrich. Pyrrole was distilled by vacuum distillation and used for the reaction. HPLC grade solvents were used for UV-Vis., CV and PL analysis.

Physical measurement

The proton (^{1}H), carbon (^{13}C) and phosphorous (^{31}P) NMR were recorded on Brucker Avance NEO instrument at 400MHz, 100MHz and 162MHz respectively. All the NMR spectra were recorded at room temperature using $CDCl_3$ and DMSO-d_6 as solvents according to their solubility. TMS was used as an internal standard for ^{1}H and ^{13}C NMR and phosphoric acid as an internal standard for ^{31}P measurement. The molecular ion peak of P(V) corroles and P1+ F^- complex has been analysed by ESI mass spectrometry (LCMS, 6230BOTF, positive mode). FT-IR measurements were done by using SHIMADZU, IRTRACER 100 in ATR mode.

Electronic and electrochemical characterisations

The UV-Vis. spectrum was measured in double beam UV spectroscopy (LMPS-UV1900S) using a quartz cuvette (1cm path length) and all the titrations were done by using DCM as solvent. Emission measurements and titrations also been studied in DCM. Fluorescent spectrometer (FP-8300) was used to analyse the photoluminescence behaviour of the catalysts using acetonitrile as solvent. The fluorescent lifetime measurement of the excited state was done by a photoluminescence spectrometer (FLS100). The electrochemical experiments (OrigaLys) were done by using an electrode system containing glassy carbon (working electrode), platinum wire (supporting electrode), Ag-AgCl (reference electrode) and 0.1M tetrabutylammonium hexafluorophosphate as supporting electrolyte in DCM.

DFT calculation

The electronic structure of the phosphorous corroles was optimized using the Gaussian 16 program. The structural optimization and TD-DFT calculations were performed with the hybrid Bocke's 3-parameter Lee-Yang-Parr level of theory (B3LPY). The Pople's 6-31G(d,p) basis set was used for all atoms present.[30,31]

Synthesis of Phosphorous corrole [P1 and P2]

The free base corroles were synthesised by following the reported procedure[32,33] To synthesis P1, 5,10,15-tris(4-cyanophenyl) corrole was dissolved in degassed pyridine, followed by the careful addition of $POCl_3$ and refluxed for 30 minutes. After completion of the reaction, the solvent was removed and the crude was subjected to column chromatography to get pure P1 as a pink solid. P2 is also synthesised by the above-mentioned procedure by using the ligand 5,15-di(4-cyanophenyl)-10(1-pyrenyl)corrole.

Spectroscopic data of P1: Yield 81%. Chemical formula [$C_{40}H_{22}N_7O_2P$]. UV-Vis. (DCM): λ_{max}(ε); 416 (57076), 523 (5000), 560 (7307), 596 (15307). FT-IR (cm^{-1}): 3442 (ν_{O-H}), 2922 ($\nu_{C=C}$),2227 ($\nu_{C\equiv N}$), 1602 ($\nu_{C=N}$), 1072 (ν_{C-N}), 825 (δ_{C-H}), 561 (ν_{P-O}).^{1}H NMR (400 MHz, DMSO-d_6) δ 9.42 (d, *J* = 6.5 Hz, 2H), 8.93 (t, *J* = 8.0 Hz, 2H), 8.85

View Article Online
DOI: 10.1039/D5NJ02527C

(d, *J* = 7.4 Hz, 2H), 8.68 (d, *J* = 7.4 Hz, 2H) 8.43 (d, *J* = 8.1 Hz, 4H), 8.32 (s, 8H), -0.93 (s, 2H). ^{31}P NMR (162 MHz, DMSO-d_6): δ -189 (s). ESI mass: m/z (Calcd. 663.16) 630.95. $[(M-2OH+H)]^+$.

Spectroscopic data of P2: Yield 79%. Chemical formula $[C_{49}H_{27}N_6O_2P]$. UV-Vis. (DCM): λ_{max}(Ɛ) 412 (60615), 523 (7461), 561 (11384), 598 (22000). FT-IR (cm^{-1}): 3443 (ν_{O-H}), 2920 ($\nu_{C=C}$),2227 ($\nu_{C\equiv C}$), 1600 ($\nu_{C=N}$), 1070 (ν_{C-N}), 823 (δ_{C-H}), 551 (ν_{P-O}). ^{1}H NMR (400 MHz, DMSO-d_6) δ 9.41 (d, *J* = 6.6 Hz, 2H), 8.87 (d, *J* = 7.5 Hz, 2H), 8.80 (s, 2H), 8.68 (d, *J* = 7.9 Hz, 1H), 8.58 (d, *J* = 4.1 *Hz*, 1H), 8.52 (d, *J* = *9.1 Hz*, 1H), 8.45 (s, 5H), 8.30 (d, *J* = 8.5 Hz, 6H), 8.23 (d, *J* = 7.4 Hz, 1H), 8.13 (d, *J* = 15.3 Hz, 1H), 7.81 (s, 1H), 7.53 (d, *J* = 9.3 Hz, 1H), 7.39 (d, *J* = 13.3 Hz, 1H), -0.64 (d, *J* = 3.6 Hz, 1H), -0.82 (s, 1H). ^{31}P NMR (162 MHz, DMSO-d_6): δ -189 (s). ESI mass: m/z (Calcd. 762.19) 761.1. $[M-H]^+$.

Results and discussion

Synthesis, characterisation and structural optimization. The free base corrole ligands and the Phosphorous corroles P1 and P2 were synthesised by following the reported procedure. [32,33] The solution of free base corrole in pyridine was degassed and followed by the drop-wise addition of $POCl_3$. The mixture was refluxed for 30 minutes and the pure phosphorous corrole (P1/P2) was obtained by column chromatography. The successful formation of the phosphorous complexes was confirmed by NMR (^{1}H and ^{31}P NMR) and ESI mass spectrum (Figure S1-S5). Both P1 and P2 show sharp ^{1}H NMR signals in the expected region. The β-pyrrolic protons of P1 appeared as four distinct signals in the range 9.42-8.68 ppm and the *meso* phenyl protons resonate at 8.43-8.32 ppm. The presence of axial hydroxy groups was confirmed by the peak at -0.93 ppm (2H), the upfield shift due to the ring current effect of corrole.[34] The β-pyrrolic protons of P2 resonated in the range of 9.41–8.84 ppm, while the β-pyrrolic protons, phenyl protons, and one pyrenyl proton exhibited overlapping signals at 8.45–8.30 ppm. The pyrene protons displayed characteristic resonances at 8.68–8.82 ppm (3H) and 8.23–7.39 ppm (5H). The axial -OH group in P2 exhibits two distinct NMR signals at -0.65 ppm and -0.82 ppm, indicating the symmetry disruption caused by pyrenyl unit. The ^{31}P NMR shows the peak at -189.41 and -189.11 ppm for P1 and P2 respectively, which confirms the P(V) centre. The ESI mass spectrum of P1 showed a peak centered at m/z 630.9 corresponding to the $[(M-2OH+H)]^+$ peak. The molecular ion peak of P2 was centered at m/z 761.1, corresponding to the $[M-H]^+$ peak.

The optimized geometries of P1 and P2 were obtained by DFT calculation using B3LYP/631G(d,p) levels. The energetically minimized structures and their side view are shown in Figure S6 and a few selected wavelengths are listed in Table S1. The observation on the meso-phenyl ring shows that the pyrene unit in P2 is orthogonally oriented to the corrole core unit when compared to the phenyl unit in the P1 corrole. The energy level diagram shows energetically well-separated Frontier orbitals. The topologies show symmetric HOMO and asymmetric LUMO orbitals in both P1 and P2. The π electron cloud occupied the entire molecule in the HOMO-LUMO molecular orbitals. On close observation, the HOMO contains electron density on the corrole core and in LUMO, it is occupied on the corrole core as well as 5, 15 meso-phenyl rings.

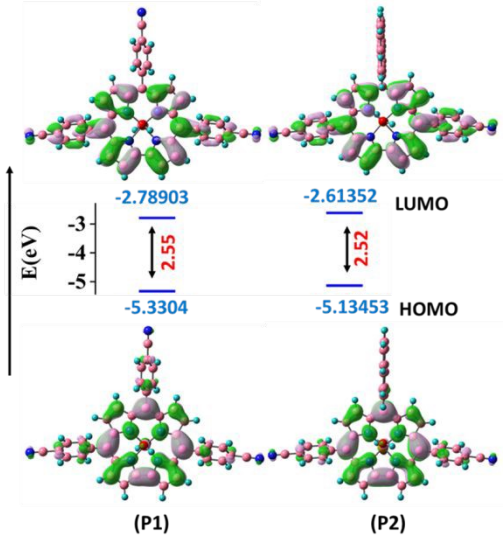

Figure 1: HOMO-LUMO energy level diagram of P1 and P2.

Photophysical studies. The absorption and emission measurements were analysed in different solvents (Figure S7). The absorption and emission wavelengths, molar absorptivity and Stokes shifts are listed in Tables S2 & S3. The Soret band appeared in the range of 415-422 nm for P1 and 412-422 nm for P2. The energetically lower Q bands were shown characteristics peak in the range of 523-605 nm for both P1 & P2. The former range is attributed to the higher-energy and more allowed Soret band and the latter to lower energy and symmetry-forbidden Q bands of the corrole core. Along with a typical absorption profile of corrole, π-π* transition of pyrene was obtained at a shorter wavelength (238–337 nm) for P2. All the peaks including π-π* transition of pyrene red shifted in highly polar DMF. Concentration-dependent UV-Vis. and emission studies were carried out for the P2 molecule to explore the excimer properties, and it was not prominent due to the higher intensity Soret band at the excimer expected region. The band assigned to the transition of pyrene was not perturbed significantly and can be attributed to the orthogonal orientation of the pyrene units concerning that of the corrole molecular plane.[35] The TD-DFT calculations were carried out to get deeper insights into the electronic transitions. The theoretically obtained absorption spectrum well correlated with the experimental spectrum (Figure S8a & 8b). The major transitions and their respective oscillator strengths are given in Table S4. The major contributions of the possible transitions revealed that non-Gouterman orbitals are also involved in the electronic transitions. The emission spectrum of P1 and P2 in different solvents shows an emission peak along with red-shifted vibrational shoulder band. The emission profile shows an emission peak in the range of 603-614 nm and a shoulder peak in the range of 660 to 674 nm for the compounds P1 & P2 respectively. The Stokes shift between the week Q band and the emission maxima depicts that the emission is fluorescence in nature and not phosphorescence. The emission behaviour of P1 and P2 was investigated under nitrogen atmosphere

at a low temperature of –10 °C (Figure S9). No new emission peaks were observed, indicating the absence of phosphorescence under these inert and low-temperature conditions. To get deeper insight into the photophysical properties, time-resolved fluorescent decay measurements were carried out in DCM. -Both P1 and P2 fitted to a single exponential decay and the excited state lifetime of P1 was calculated as 3.2 ns and 3.1 ns for P2 (Table S5).

Photo-bleaching experiment:

The photostability of P1 and P2 was evaluated via photo-bleaching experiments. Solutions of P1 and P2 in DCM were irradiated with blue LED light (100 W, total light dosage: 180 J cm^{-2}) for 30 minutes. The changes in the Soret band absorption were monitored using UV-Vis. spectroscopy.

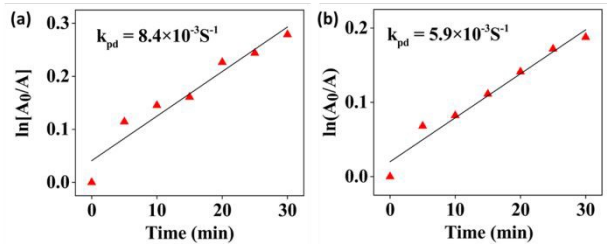

Figure 2: Photo-bleaching graph of time vs. $\ln(A/A_0)$ for P1(a) and P2(b).

The photodegradation rate constants were determined from the slope of the plot of irradiation time *vs.* $\ln(A_o/A)$ (Figure 2). The photodegradation quantum yield was calculated as 2.0 for P1 and 1.6 for P2 using equation 2.1. A comparative analysis of the photodegradation rate constants and photodegradation quantum yields indicates that P2 exhibits superior photostability relative to P1. This enhanced stability is attributed to the extended π-conjugation of pyrenyl unit.[36]

Electrochemical studies. The redox behaviour of compounds P1 and P2 was investigated by cyclic voltammetry (CV) and differential pulse voltammetry (DPV) using DCM as solvent and $TBAPF_6$ (0.1M) as the supporting electrolyte. Electrochemical measurements were performed at a scan rate of 100 mVs^{-1}. The anodic and cathodic peak potentials are summarized in Table 1. Both P1 and P2 exhibited irreversible first oxidation processes, occurring at +0.92 V and +0.88 V, respectively, while their first reduction was found to be reversible, with potentials at –0.97 V and –0.98 V, respectively (Figure S10). The minimal variation observed in these redox potentials suggests that the nature of the 10-meso substituents exerts only a marginal influence on the redox characteristics of P(V) corroles. Moreover, the experimentally derived HOMO–LUMO energy levels and the associated electrochemical energy gaps (ΔE) showed agreement with theoretical predictions.

Table 1: Oxidation, reduction potential of corrole, Electrochemical energy levels and energy differences.

Corrole	E_{ox}	E_{red}	E_{HOMO}[a]	E_{LUMO}[b]	ΔE^c
P1	+0.92, +1.40, +1.8	-0.97, -1.71	-5.28	-3.66	1.62
P2	+0.88, +1.43, +1.76	-0.98, -1.69	-5.24	-3.88	1.46

[a]E_{HOMO} = - [(E_{ox} - $E_{1/2}$(ferrocene)) + 4.8]; [b]ELUMO = - [(E_{red} - $E_{1/2}$(ferrocene)) + 4.8]; ΔE^c = HOMO-LUMO.

Colorimetric response. Owing to the pronounced chromatic sensitivity of the corrole chromophore toward various binding species, numerous corrole-based colorimetric sensors have been developed. Consequently, it is important to evaluate the colorimetric response of P(V) corroles toward a range of anionic analytes. Given that P(V) corroles contain electron-withdrawing *meso*-phenyl substitutes, we speculated that this characteristic could enhance its binding affinity toward anions. In this context, receptors P1 and P2 were systematically tested against a panel of anions, including Cl^-, I^-, NO_3^-, CN^-, HPO_4^{2-}, Br^-, OH^-, and F^- in DCM at RT. All the anions were taken as their tetra butyl ammonium salts. Notably, the addition of F^- ions induced a distinct and rapid color transition from pinkish-violet to green (Figure 3).

Figure 3: Colorimetric response of (a) P1 and (b) P2 towards various anions.

Optical spectroscopy. Following the initial colorimetric screening, the interaction between phosphorus(V) corroles and F^- was thoroughly examined through UV–Vis. spectroscopic titrations. The titration data indicated a slight attenuation in the Soret band intensity, while significant spectral changes were evident in the Q-band region, including a pronounced bathochromic shift. The Soret band of P1 exhibits a bathochromic shift of 10 nm upon the addition of 8 equivalents of F^-, whereas in the Q-band region, the absorption maximum shifts from 592 nm to 604 nm (Figure S11). P2 displays a similar pattern of spectral changes, with the Soret band shifting from 411 nm to 421 nm and the intense Q-band also red-shifting to 604 nm (Figure 4). These spectral changes in P2 reach saturation upon the addition of 13 equivalents of F^-. These observable spectral transitions strongly suggest the formation of a stable complex between the corrole receptor and the F^- ion. The red shift can be attributed to two key factors: (1) charge-transfer interactions between the electron-deficient corrole macrocycle and the electron-rich F^- anion, and (2) the formation of a ground-state complex.[37]
The experimental findings are further compared with the theoretical outcomes. The HOMO-LUMO energy levels indicate that the P(V)

View Article Online
DOI: 10.1039/D5NJ02376

corrole + F^- adducts reside at a higher energy Slevel compared to the P(V) corroles, suggesting reduced stability and enhanced chemical reactivity of the adducts (Figure S12 & Table 2). Examination of the HOMO–LUMO energy gap reveals that the decreased band gap observed after anion additions, correlates well with the bathochromic shift detected in the experimental UV–Vis. spectra.

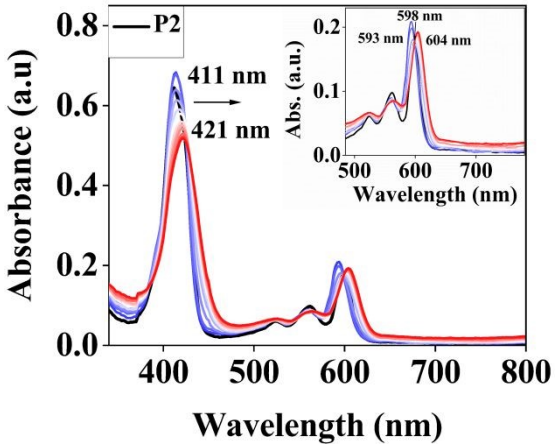

Figure 4: Absorption changes of P2 upon F^- addition; inset shows changes in the Q band region.

Furthermore, the coordination of F^- ions to the sensing probe induced an increase in polarization, as evidenced by a notable rise in the dipole moment upon complexation.[38] The electronic transitions of P(V) corrole + anion adducts were obtained from the TD-DFT analysis, the major transitions and the respective oscillator strengths were listed in Table S4. The theoretical UV-Vis. spectrum also exhibits the red shift in the Q band as shown in Figure S8c & 8d.

Table 2: HOMO / LUMO energy levels, energy difference, total energy and dipole moment.

Corrole	HOMO	LUMO	[a]ΔE	Total energy / Hartree	Dipole moment
P1	-5.3304	-2.7890	2.55	-2412.6	4.93
P1+F-	-2.3863	-0.0348	2.34	-2512.5	5.67
P2	-5.1345	-2.6135	2.52	-2703.9	2.50
P2+F-	-2.2720	-0.0318	2.23	-2803.8	7.05

[a]ΔE = HOMO - LUMO

Fluorescence experiments. Figures 5a & S13a show the spectrum of P(V) corroles with the gradual addition of F^- in DCM. P1 and P2 show emission peak maxima at 608 nm and 610 nm respectively. The gradual addition of F^- to the P(V) corroles leads to a decrease in the fluorescence intensity along with a 5 nm blue shift. The decrease in the emission intensity owing to the adduct formation between the electron-rich anions and the P(V) corrole. The quenching in emission intensity of P1 attained saturation at 4.5×10^{-5}M F^- concentration and P2 attained saturation at 5.5×10^{-5}M concentration of F^-. The inset graph shows the linear relationship between [F-] and I/I_0 (figure 5a & S13a). The shift in the emission wavelength is not involved in the emission color change, which accorded well with the chromaticity plot (Figure 5b & S13b). The titre values obtained from the fluorescence titration and the corresponding anion concentrations were used to construct the Benesi–Hildebrand plot (Figure 6a & S 13c). A graph of 1/[M] versus $1/[I_0 - I]$ was plotted, and the association constants (K_a) were calculated using Equation 2.2. The calculated K_a values are 4.1×10^3 for the P1+F^- titration and 6.3×10^3 for the P2+F^-. The significant difference in the association constants indicates strong binding interactions between the P(V) corrole and the anion.

For practical relevance, a sensor must exhibit high sensitivity, capable of detecting even trace levels of the target analyte. In this context, the LOD was determined by plotting the variation in emission intensity as a function of increasing anion concentration. The slope of the linear region of the plot was used to calculate the LOD based on Equation 2.3. The calculated LOD and LOQ are summarized in Table 3. The LOD was found to be 0.101 ppm for P1 and 0.089 ppm for P2, both of which are significantly lower than the permissible F^- intake limit established by the WHO (100.7–150.1 ppm).[39] These results demonstrate that P1 and P2 possess high sensitivity for F^- detection, as evidenced by their low LOD values and high K_a.

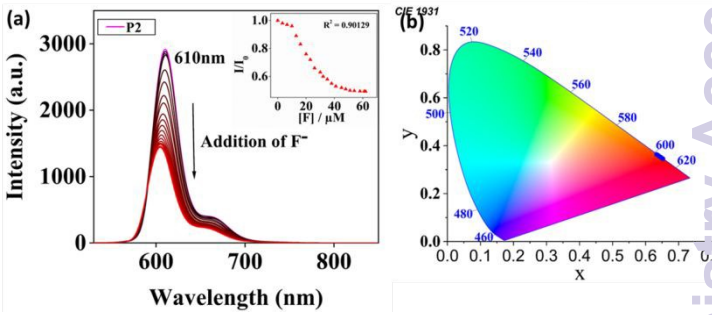

Figure 5: (a) Changes in emission spectrum of P2 upon F^- addition; inset shows graph of $[F^-]/\mu M$ vs I/I_0; (b) Chormtacity diagram of fluorometric titration of P2.

The changes in the emission spectra of P1 and P2 upon the introduction of various anions was investigated. Notably, only F^- ions induced a significant quenching of emission intensity, demonstrating the high selectivity of P1 and P2 for F^- sensing (Figure 6b & 6c). Competitive experiments were performed to know the interference of various anions. The fluorescence quenching behavior of F^- was evaluated in the presence of various competing anions. The emission quenching induced by F^- remains unaffected, indicating negligible interference from other anions and confirming the high sensitivity of the system toward F^- ions (Figure 6d & S13d). Since the detection limits of these receptors are significantly lower than the WHO standards, their performance was evaluated in comparison to previously reported fluoride sensors for better assessment (Table 4). The comparison table clearly shows that the synthesized phosphorus-based corrole probes offer better fluoride sensing performance.

Table 3: Association constant, LOD, LOQ and binding ratio of P(V) corroles + F^- adduct.

Corrole	Association constant (Ka)	LOD / µM (ppm)	LOQ (µM) / (ppm)	Binding ratio
P1+F⁻	4.1×10^3	0.39 (0.101)	1.18 (0.545)	1:1
P2+F⁻	6.3×10^3	0.34 (0.089)	0.44 (0.206)	1:1

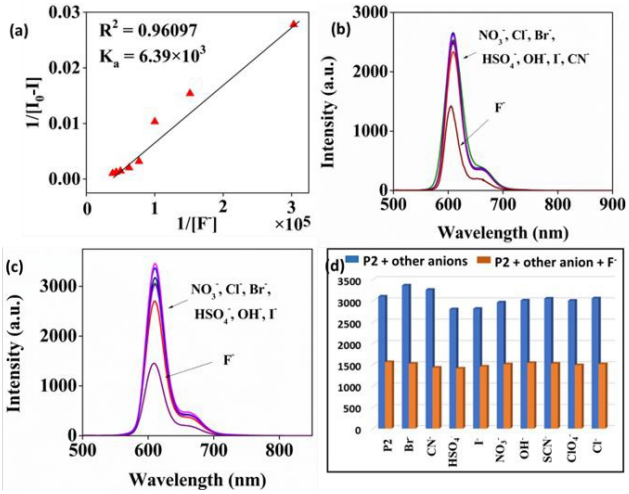

Figure 6: (a) B-H plots obtained from emission spectral data for P2. Changes in the emission spectrum of (b) p1 and (c) P2 with the addition of various anions. (d) Interference effect of various anions on the emission intensity of P2.

Effect of F⁻ sensing under various environmental conditions and recyclability. The stability and reliable sensing ability under different environmental conditions, such as varying temperatures, exposure to visible light, and reversibility make P1 & P2 suitable for practical applications. Photostability was evaluated under blue light irradiation, chosen due to the strong absorbance of corrole complexes in the blue region. P1 / P2 with a concentration of 0.013 mM was exposed to 50 W blue LED light for 30 minutes. Absorption changes were periodically monitored at 5-minute intervals using UV-Vis. spectroscopy. Following each interval, F⁻ was introduced to assess the retention of sensing capabilities. The plot of absorption at the Soret band versus time confirmed negligible variation, indicating excellent photostability and sustained F⁻ sensing performance after light exposure (Figure 7a & S14a). Thermal stability was also assessed by subjecting the corrole probes dissolved in DCM to a temperature range from 20°C to 50°C. UV-Vis. analysis revealed consistent absorbance across the tested temperatures, confirming thermal robustness. Furthermore, upon F⁻ addition, both visual and spectroscopic changes uphold the high sensitivity and responsiveness of the P(V) corroles under the examined conditions (Figure 7b & S14b). The addition of a few drops of water to the P1/P2 + F⁻ complex caused an immediate and reversible transformation back to the P1/P2 corroles. This reversible behaviour was clearly confirmed through both colorimetric changes and spectroscopic analysis, as shown in the corresponding figures (Figure 7c & S14c).

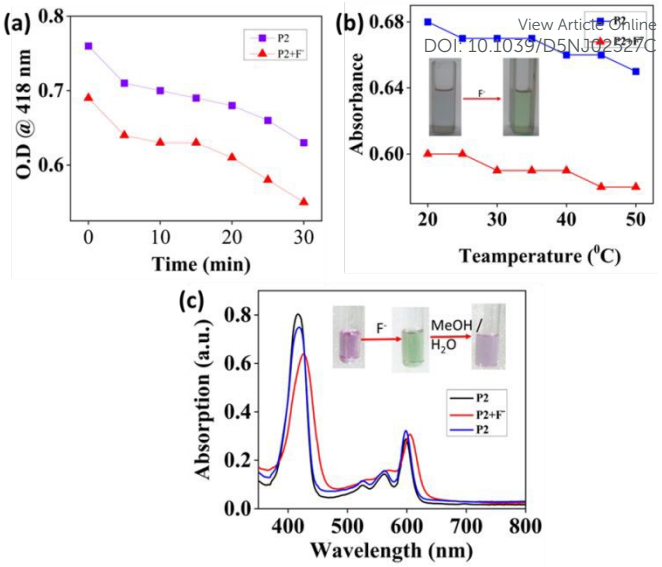

Figure 7: (a) Change in the Soret band of P2 before and after the addition of F⁻ under light irradiation. (b) Stability of P2 at various temperature (20 to 50°C). (c) Reversibility P2 +F⁻ adduct by the addition of H_2O / MeOH.

Table 4: Comparison table of LOD value with previously reported literature.

Chemosensor	Method	LOD / µM	Application	Ref.
3-acetylcoumarin based carbazones	Colourimetric / Fluorometric	0.63	Test trips, Solid state and logic gate	40
Polyacrylate functionalized Gold NP	Colourimetric / Fluorometric	18	Toothpaset & water sample	41
ortho-azonaphthol polymer	Colorimetric / Flurometric	0.96 & 2.55	-	42
Anthraimidazoledione based compounds	Colourimetric / Fluorometric	0.57 – 0.98	Test strip	43
Ceriumoxide NP	Colourimetric / Fluorometric	0.64	Toothpaste / water sample	44
Organolead halide pervoskite quantum dots	Fluorometric	3.2	-	45
Hydroxyaryl Schiff base based compund	Colourimetric / Fluorometric	0.5	-	46
Al3+ complex of	Colourimetric /	2.64	-	47

chlorophospho nazo III	Fluorometric			
Phosphorous(V) corroles	Colourimetric / Fluorometric	0.36 & 0.34	Solid-state sensor/ smartpho ne-assisted sensing	This work

Mechanism. The fluorescence quenching observed in P1 and P2 is primarily attributed to ground-state complex formation between the corrole receptor and the F^- anion, which was evident from the change in UV-Vis. spectrum upon anion addition. The quenching mechanism may proceed via either static or dynamic pathways. The Stern-Volmer graph was plotted between I_0/I vs. [F^-]. S-V plots display a linear correlation between the I_0/I ratio and increasing F^- concentration, suggesting a static quenching process (Figure S15). To further confirm, time-resolved fluorescence measurements were performed in DCM, both in the absence and presence of F^- ions (Figure 8a). Static quenching does not affect the fluorescence lifetime, whereas dynamic quenching involves a change in the lifetime. The fluorescence decay curves for the P (V) corrole and the F^- adducts were well-fitted to a single-exponential decay profile, and the excited-state lifetimes did not show any pronounced difference (Table S5), confirming that the quenching is static in nature. Moreover, static quenching typically does not result in significant bathochromic shifts in the absorption spectra of the receptor. Consistently, UV-Vis. titration experiments of P(V) corroles with F^-revealed only minor redshifts in the Soret and Q bands.[48]

The binding stoichiometry between the P(V) corrole and F^- was determined using Job's plot analysis. Although a 1:2 binding mode was initially anticipated due to the two possible axial coordination sites, the molar fraction at 0.5 indicated a 1:1 binding ratio between the P(V) corroles and the F^- (Figure 8c & S16a). Supramolecular chemosensors typically operate through interactions such as hydrogen bonding, acid-base interactions, and anion–π interactions. In this system, the observed colorimetric and fluorometric responses may result either from the replacement of axial -OH by the addition of F^- [P(V)corrole-F] or hydrogen bonding between the axial –OH group of the P(V) corrole and the F^- ion [P(V)corrole(OH)…F]. The regeneration of the sensing probe upon the addition of water or methanol to the P(V) corrole–anion complex not only demonstrates the reversibility of binding but also supports the involvement of hydrogen bonding interactions between the P1/P2 and F^- (Figure 9). The ESI mass spectrum of the P1+F^- adduct in DCM shows a peak at m/z 680.5 corresponding to the hydrogen-bonded complex [P(V)corrole(OH)…F] (Figure 8b). The ESP diagram was obtained from the DFT analysis. The possibility of F^- binding to the axial -OH was evidenced by the potential mapping (Figure S17).

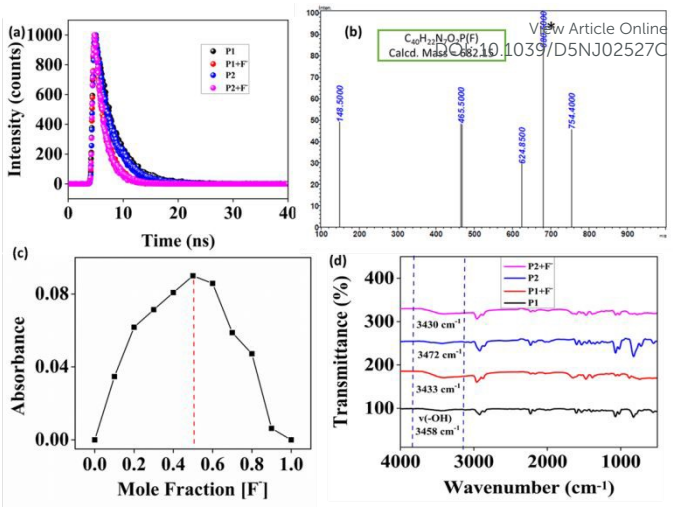

Figure 8: (a) Time-resolved fluorescence decay spectrum of P(V) corroles before and after F^- addition. (b) ESI mass spectrum of P1+F^- (c) Job's plot for the complex formation between P1 + F^-. (d) FT-IR spectrum P (V) corrole, before and after the F^- addition.

The FT-IR spectra were recorded to gain further insight. After F^- addition, a broadening of the –OH stretching peak was observed along with a slight shift to lower frequencies.[49] Specifically, for P1, the –OH stretching frequency shifted from 3458 cm^{-1} to 3433 cm^{-1}, and for P2, from 3472 cm^{-1} to 3430 cm^{-1} (Figure 8d). Electrochemical studies were also conducted in DCM at room temperature. During electrochemical titration, an anodic shift in the oxidation potential was observed, with the oxidation peak moving from 0.8 V to 1.0 V upon 0 to 4 equivalents of F^- addition (Figure S16b). These spectral changes provide additional evidence for hydrogen bonding interactions between the P(V) corrole and the F^- anion.

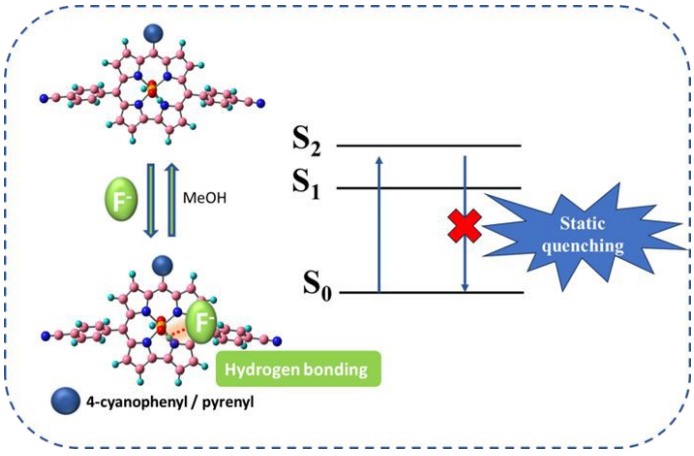

Figure 9: Schematic representation of sensing mechanism.

Real-time applications

Solid state F- detection. To investigate the practical applicability the solid-state detection of F^- was achieved using silica gel as a substrate. The sensor P1/P2 was dissolved in DCM and added to silica gel (100-200 mesh size) and evenly distributed. Exposure to a DCM solution containing F^- ions, the colour changed from pinkish

violet to green and the fluorometric changes were evidenced by quenching emission as illustrated in Figure 10a.

Smartphone-assisted fluoride sensing. Although the presence of F^- ions can be visually detected through perceptible color changes, quantitative analysis typically necessitates cost-intensive spectrometric techniques. Given the distinct colorimetric response of P(V) corroles upon F^- binding, a smartphone-assisted colorimetric detection method was employed, following a previously established protocol.[50,51] Incremental volumes of F^- solution (0.25 – 2 equivalents) were added to 30 µM solution of P1 in DCM, and the resulting color changes were captured using a smartphone camera for each addition. The corresponding RGB values for each color transition were extracted using a freely available RGB detector application. Each image was uploaded to the application to determine the RGB values. Visual observation alone is inadequate for precise analysis; therefore, a calibration curve was constructed using RGB measurements at varying F^- concentrations. The plotted data revealed a linear correlation for the G/B ratio versus $[F^-]$ (R^2 = 0.9628) (Figure 10b). The detection limit was calculated using the slope of the linear regression. An analogous approach was adopted for P2, where the G/B ratio versus F^- concentration was similarly evaluated to assess its detection performance (Figure S18). The LOD was calculated as 404 µM for P1 and 301µM for P2.

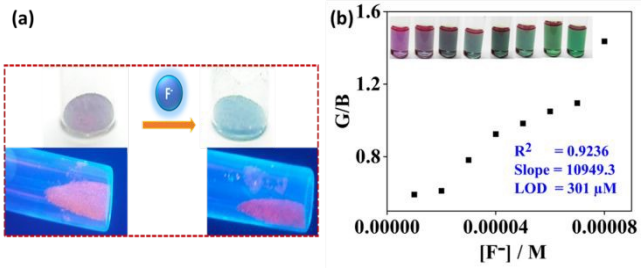

Figure 10: (a) solid-state sensor of P2; colorimetric (top) and fluorometric (bottom) changes by F^- addition (b) Graph of $[F^-]$ in P2 solution vs. G/B; the inset figure represents the color by the addition of F^-.

Reactivity as catalysts. Phosphorus corroles are well-documented for their photosensitizing properties and ability to generate reactive oxygen species (ROS). Accordingly, the synthesized P(V) corroles were evaluated for their catalytic performance in the blue light-induced sulfoxidation of thioanisole (Scheme 1). Thioanisole (0.4 mmol) and P(V) corrole (1 mol%) were taken in a 10 ml test tube, dissolved in 0.25 ml of DCM followed by the addition of 2ml ethanol and the reaction mixture was closed with the septum and stirred under blue light exposure, the sulfoxide formation was confirmed by ^1H and ^{13}C NMR analysis (Figure S19 & S20). Both P1 and P2 exhibited efficient catalytic activity under visible light irradiation. In acetonitrile, only 45% conversion of thioanisole was observed, whereas complete substrate consumption occurred in ethanol (< 70%). P2 demonstrated superior catalytic efficiency compared to P1, primarily due to its enhanced photostability and greater singlet oxygen generation, attributed to the extended π-conjugation conferred by the pyrene moiety. The singlet oxygen quantum yield was determined using a direct method with DPBF as a singlet oxygen scavenger. A mixture of P(V) corrole (P1 or P2) and DPBF was irradiated with red light (650 nm), and the resulting decrease in DPBF absorbance was monitored over time (0-50 s). The reduction in absorbance correlated directly with the amount of $^1O_2$ produced. The calculated singlet oxygen quantum yields for P1 and P2 were 22.5% and 27%, respectively, supporting the better catalytic performance of P2. Complete substrate conversion was achieved within 7 hours under optimal conditions.

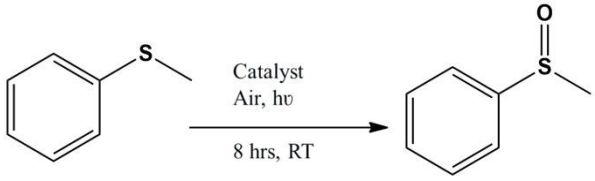

Scheme 1: Sulfoxidation of thioanisole

Control experiments conducted in the absence of light or catalyst showed no product formation, highlighting the indispensable roles of both photocatalysts and light in the reaction. Additionally, reactions carried out under a nitrogen atmosphere resulted in no observable product, underscoring the essential involvement of molecular oxygen. The reaction proceeds well without the addition of any chemical oxidants, suggesting that atmospheric oxygen acts as the sole oxidant in this transformation (Scheme 2).

To investigate the involvement of singlet oxygen in the reaction mechanism, quenching experiments were performed. Various radical quenchers including DMSO, DABCO, sodium azide and benzoquinone were subjected to the optimised reaction condition. In the presence of DMSO and benzoquinone, only a minimal suppression of sulfoxidation was monitored.

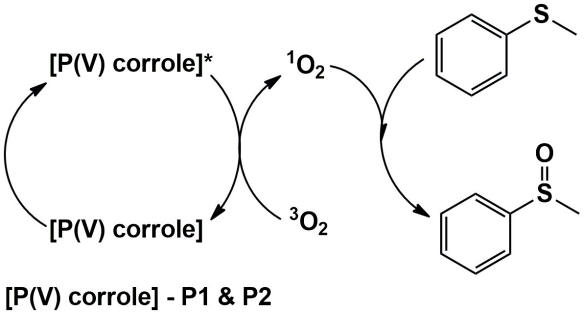

Scheme 2: Proposed mechanism of sulfoxidation.

The addition of 2 equivalents of singlet oxygen quenchers, such as DABCO and sodium azide to the standard reaction conditions resulted in significant suppression of sulfoxide formation, indicating that the oxidation proceeds via a singlet oxygen-mediated pathway (Scheme 2). Notably, even upon extending the reaction duration to 24 hours, no further oxidation of the sulfoxide to sulfone was detected, demonstrating selectivity in the product formation.

Conclusions

In conclusion, we have developed two phosphorus(V) corrole derivatives (P1 and P2) and investigated their dual functionality as fluorescent sensors for F^- detection and as photocatalysts for

DOI: 10.1039/D5NJ02527C

sulfoxidation reactions. Both derivatives exhibited high sensitivity and selectivity toward F^- detection via colorimetric and fluorometric responses. The sensing mechanism was identified as static fluorescence quenching, supported S–V plot and time-resolved fluorescence decay results. The mode of interaction between P1/P2 and F^- was established to involve hydrogen bonding, as corroborated by ESI-MS, FT-IR, and DFT studies. The stability and performance of the P(V) corroles under various environmental conditions affirm their practical applicability. Notably, their detection efficiency was demonstrated in both solution and solid-state formats, including silica gel-based assays and cost-effective, smartphone-assisted RGB analysis highlighting their promise for real-world sensing applications. Furthermore, the strong fluorescence and photostability of the P(V) corroles enabled their application as efficient photocatalysts for the oxidation of thioanisole. The reaction was conducted under mild conditions, employing ethanol as a solvent, visible light as an energy source, and atmospheric oxygen as the oxidant. Ongoing research is focused on expanding the substrate scope and application of this methodology to diverse oxidation reactions, including those involving oxygen atom transfer (OAT).

Conflicts of interest

There are no conflicts to declare.

Acknowledgements

The authors are very grateful for the financial support from the DST-SERB (grant number SB/FT/CS-093/2012) and TARE–SERB (grant number TAR/2023/000464). MM thankfully acknowledge central instrumental facilities at SRM IST, PNCF HPCC and IITM. GD acknowledge SRM IST for the research fellowship.

References

1. Y. Ding, W.-H. Zhu and Y. Xie, *Chem. Rev*., 2017, **117**, 2203–2256.
2. Z. Ullah, S. Subramanian, H. Lim, N. A. Dogan, J. S. Lee, T. S. Nguyen and C. T. Yavuz, *ACS Appl. Mater. Interfaces*, 2025, **17**, 17767-17774.
3. L. Yang, M. Li, S. Ruan, X. Xu, Z. Wang and S. Wang, *Spectrochim. Acta, Part A*, 2021, **255**, 119718.
4. R. Kubba, O. Yadav, S. Maji, N. Fridman and A. Kumar*, J. Mol. Struct.*, 2022, **1269**, 133780.
5. K. Yu, Q. Wang, W. Xiang, Z. Li, Y. He and D. Zhao, Inorg. Chem., 2022, **61**, 13627–13636.
6. L. Yang, Y.-L. Liu, C.-G. Liu, Y. Fu and F. Ye, *J. Mol. Struct.,* 2021, **1236,** 130343.
7. J. Park, S. H. Kim, J.-Y. Cho, S. R. Atriardi, J.-Y. Kim, H. Mardhiyah, B. Y. Park and S. K. Woo, *Green Chem.,* 2025, **27**, 3284–3292.
8. C.-L. Li and X.-F. Wu, *Chem. Transform. C1 Compd*., 2022, **3**, 1647–1665.
9. M. C. Carreño, G. H. Torres, M. Ribagorda, A. Urbano, *Chem. Commun.,* 2009, **41,** 6129-6144.
10. J. Corpas, S.-H. Kim-Lee, P. Mauleón, R. Gómez Arrayás and J. C. Carretero, *Chem. Soc. Rev.,* 2022, **51**, 6774–6823.
11. A. M. Saleh, A. M. El-Kosasy and N. V. Fares, *Egypt. J. Chem.*, 2023, **66,** 141–148.
12. M. Janeta and S. Szafert, *Inorg. Chem. Front*., 2025, https://doi.org/10.1039/D5QI00323G.
13. P. Thiruvengetam and D. K. Chand, *J. Indian Chem. Soc*., 2018, **95**, 781–788.
14. B. Sreedhar, P. Radhika, B. Neelima, Neha Hebalkar, A.K. Mishra, *Catal. Commun*., 2008, **10**, 39-44.
15. Q. Pu, M. Kazemi and M. Mohammadi, *Mini-Rev. Org. Chem.,* 2020, **17**, 423–449.
16. C. Ye, Y. Zhang, A. Ding, Y. Hu and H. Guo, *Sci. Rep*., 2018, **8**, 2205.
17. C. Zahn, T. Stensitzki, A. Berg, A. Mahammed, A. Zacarias, Z. Gross and K. Heyne, *Phys. Chem. Chem. B*, 2021, **125**, 10571–10577.
18. C. M. Lemon, S. J. Hwang, A. G. Maher, D. C. Powers and D. G. Nocera, *Inorg. Chem.*, 2018, **57,** 5333–5342
19. S. y. Huang, G. Yang, Z.-d. Liang, L. Zhang, F. l. Zhao and H.-Y. Liu, *J. Phys. Chem. C*, 2025, **129**, 8966–8973.
20. W. Sinha, N. Fridman, A. Mahammed and Z. Gross, *Isr. J. Chem.*, 2023, **63**, e202300036.
21. T. Stensitzki, Y. Yang, A. Berg, A. Mahammed, Z. Gross and K. Heyne, *Struct. Dyn.*, 2016, **3,** 043201.
22. Y. Han, Y.-M. Lee, M. Mariappan, S. Fukuzumi and W. Nam, *Chem. Commun.*, 2010, **46,** 8160–8162.
23. A. Varshney, D. Ahluwalia, R. Kubba and A. Kumar, *J. Indian Chem. Soc.*, 2022, **99**, 100708.
24. C. I. M. Santos, E. Oliveira, J. F. B. Barata, M. A. F. Faustino, J. A. S. Cavaleiro, M. G. P. M. S. Neves and C. Lodeiro, *J. Mater. Chem.*, 2012, **22**, 13811–13819.
25. E. Jaworska, F. Caroleo, C. Di Natale, K. Maksymiuk, R. Paolesse and A. Michalska, *J. Porphyrins Phthalocyanines*, 2020, **24**, 929–937.
26. A. D'Andrea, G. Pomarico, S. Nardis, R. Paolesse, C. Di Natale and L. Lvova, *J. Porphyrins Phthalocyanines*, 2019, **23**, 117–124.
27. A. Mahammed, K. Chen, J. Vestfrid, J. Zhao and Z. Gross, *Chem. Sci.*, 2019, **10,** 7091-7103.
28. I. Luobeznova, M. Raizman, I. Goldberg and Z. Gross, *Inorg. Chem.*, 2006, **45**, 386–394.
29. L. M. Reith, M. Stiftinger, U. Monkowius, G. Knör and W. Schoefberger, *Inorg. Chem.*, 2011, **50**, 6788–6797.
30. Frisch, M. J.; Trucks, G. W.; Schlegel, H. B.; Scuseria, G. E.; Robb, M. A.; Cheeseman, J. R.; Scalmani, G.; Barone, V.; Petersson, G. A.; Nakatsuji, H.; et al. Gaussian 16, Revision A. 03; Wallingford CT, 2016.
31. M. J. Frisch, J. A. Pople and J. S. Binkley, *J. Chem. Phys.*, 1984, **80**, 3265–3269.

View Article Online
DOI: 10.1039/D5NJ02527C

32. B. Koszarna and D. T. Gryko, *J. Org. Chem.*, 2006, **71**, 3707–3717.
33. K. M. Kadish, Z. Ou, V. A. Adamian, R. Guilard, C. P. Gros, C. Erben, S. Will and E. Vogel, *Inorg. Chem.*, 2000, **39**, 5675–5682.
34. X. Jiang, Y.-M. Sun, J.-H. Cen, W. Yang, Y.-H. Liao, L. Shi, D.-Z. Lin and H.-Y. Liu, *ChemSelect*, 2021, **6**, 8200–8204.
35. S. Sujesh, B. Basumatary, A. Kumar and J. Sankar, *Eur. J. Inorg. Chem.*, 2021, 2021, 540–547.
36. T. V. Acunha, H. F. V. Victória, K. Krambrock, A. C. Marques, L. A. S. Costa and B. A. Iglesias, *Phys. Chem. Chem. Phys.*, 2020, **22**, 16965–16977.
37. V. V. Kumar, D. Ramadevi, V. M. Ankathi, T. K. Pradhan and K. Basavaiah, *Microchim. J.*, 2020, **157**, 105028.
38. F. J. de Lera-Garrido, V. Vázquez-Villar, M. P. Fernández-Liencres, A. Sánchez-Ruiz, A. Navarro, J. Tolosa and J. C. García-Martínez, *Dyes Pigm.,* 2024, **225**, 112035.
39. Q. Lin, Q.-P. Yang, B. Sun, J.-C. Lou, T.-B. Wei and Y.-M. Zhang, *RSC Adv.*, 2015, **5**, 11786–11790.
40. L. Yang, M. Li, S. Ruan, X. Xu, Z. Wang and S. Wang, *Spectrochim. Acta Part A*, 2021, **255**, 119718.
41. A. Kumar, M. Bhatt, G. Vyas, S. Bhatt and P. Paul, *RSC Adv.*, 2017, **9**, 17359-17368.
42. Y. Yoon, S. Jo, D. H. Lee and T. S. Lee, *Polymer*, 2022, **261**, 125421.
43. B. Bhattacharyya, A. Kundu, N. Guchhait and K. Dhara, J. *Fluoresc.,* 2017, **27**, 1041–1049.
44. B. Liu, Z. Huang and J. Liu, *Nanoscale*, 2016, **8**, 13562–13567.
45. L.-Q. Lu, M.-Y. Ma, T. Tan, X.-K. Tian, Z.-X. Zhou, C. Yang and Y. Li, *Sens. Actuators B*, 2018, **270**, 291–297.
46. A. S. Gupta, K. Paul and V. Luxami, *Sens. Actuators B*, 2017, **246**, 653–661.
47. M. Shimizu, S. Aikawa and Y. Fukushima, *Tetrahedron Lett*., 2023, **118**, 154405.
48. P. P. Gawas, B. Ramakrishna, R. Pamanji, J. Selvin and V. Nutalapati, *Mater. Adv.,* 2024, **5**, 336–348.
49. G. Kaur, G. Kumar and I. Singh, *J. Mol. Struct.*, 2025, **1319**, 139252.
50. A. Ranolia, A. Duhan, R. K. Dhaka, S. Singh, G. Joshi, P. Kumar, D. Singh, M. Wahajuddin and J. Sindhu, *RSC Adv.*, 2025, **15**, 9129–9140.
51. G. Sivakumar, A. Babu, B. Ghanti, J. Swathi, V. Nutalapati, S. Banerjee and S. Maji, *Adv. Funct. Mater.*, 2025, **35**, 2419620.

Data Availability Statement

Data available on request from the authors. The data that support the findings of this study are available from the corresponding author, upon reasonable request.